MATERIALS SCIENCE

In-sensor multilevel image adjustment for high-clarity contour extraction using adjustable synaptic phototransistors

Jong Ik Kwon[1,2]†, Ji Su Kim[3,4]†, Hyojin Seung[3,4], Jihoon Kim[3,4], Hanguk Cho[3,4], Tae-Min Choi[5], Jungwon Park[3,4], Juyoun Park[5], Jung Ah Lim[6,7,8], Moon Kee Choi[2,3]*, Dae-Hyeong Kim[3,4]*, Changsoon Choi[1]*

Robotic vision has traditionally relied on high-performance yet resource-intensive computing solutions, which necessitate high-throughput data transmission from vision sensors to remote computing servers, sacrificing energy efficiency and processing speed. A promising solution is data compaction through contour extraction, visualizing only the outlines of objects while eliminating superfluous backgrounds. Here, we introduce an in-sensor multilevel image adjustment method using adjustable synaptic phototransistors, enabling the capture of well-defined images with optimal brightness and contrast suitable for achieving high-clarity contour extraction. This is enabled by emulating dopamine-mediated neuronal excitability regulation mechanisms. Electrostatic gating effect either facilitates or inhibits time-dependent photocurrent accumulation, adjusting photo-responses to varying lighting conditions. Through excitatory and inhibitory modes, the adjustable synaptic phototransistor enhances visibility of dim and bright regions, respectively, facilitating distinct contour extraction and high-accuracy semantic segmentation. Evaluations using road images demonstrate improvement of both object detection accuracy and intersection over union, and compression of data volume.

INTRODUCTION

Recent progress in robotic vision has advanced mobile system technologies (*1*–*3*), including autonomous vehicles and unmanned aerial systems, by enabling them to capture and interpret their surrounding visual data effectively (*4*–*6*). The robotic vision sensors (e.g., high-definition cameras) generate a tremendous volume of image data, reaching up to 40 Gb s^{-1}, and these massive data are analyzed by using sophisticated data processing techniques for decision of next tasks (*7*–*9*). Such high-throughput data stream places considerable pressure on processing units, often exceeding the processing power and storage capacities of onboard systems (*10*–*12*). Consequently, there is an increasing reliance on high-performance computing solutions, particularly cloud computing, optimized for both managing vast datasets and executing complex data processing (*13*–*15*). However, there is a major bottleneck in these systems; the latency in data transmission, especially from vision sensors to remote servers (*16*), impeding prompt responsiveness and fast decision-making (*17*–*19*).

An ideal strategy for mitigating latency issues is compressing visual data into a compact format (*20*, *21*), selectively retaining only crucial information (*22*, *23*). This strategy not only reduces data volume but also facilitates high-accuracy object detection. A key technique in the data compaction methodology is contour extraction, which simplifies the image into clear and manageable contours that can be classified into semantic classes (e.g., semantic segmentation) (*24*, *25*). As a result, there have been considerable efforts on developing robust contour extraction techniques, e.g., thresholding methods and edge-detection methods, all of which target the same objective-production of clear contour-extracted images that high-performance computing solutions can accurately recognize (*26*–*28*).

This goal is closely tied to the quality of images (*29*). Well-defined images with optimal brightness and contrast through image adjustments result in facile contour extraction with minimal noise, facilitating accurate object detection as well as efficient data transmission (see fig. S1A in which contour-extracted images with different levels of image adjustment are compared). However, software-based image adjustment methods incur computational burdens (e.g., increased power consumption and data latency) on processors that should operate within limited performance capacities [fig. S1B (i)] (*30*, *31*). Regarding this issue, vision sensors based on synaptic photodetectors can present a potential solution (*32*–*34*). The synaptic photodetectors can perform contrast enhancement through in-sensor processing, e.g., amplifying critical signals and filtering out background noise (*35*, *36*), thus offering energy-efficient and high-bandwidth solutions [fig. S1B (ii)]. However, the key challenge is how to maximize visual perception accuracy across diverse environmental conditions, e.g., light-scattered sunny days and dim cloudy days.

Here, we tackle this challenge by proposing a hardware-level in-sensor multilevel image adjustment method using adjustable synaptic phototransistors, optimizing image brightness and contrast across bright and dim regions for achieving high-clarity contour

[1]Center for Quantum Technology, Post-silicon Semiconductor Institute, Korea Institute of Science and Technology (KIST), Seoul 02792, Republic of Korea. [2]Department of Materials Science and Engineering, Ulsan National Institute of Science and Technology (UNIST), Ulsan 44919, Republic of Korea. [3]Center for Nanoparticle Research, Institute for Basic Science (IBS), Seoul 08826, Republic of Korea. [4]School of Chemical and Biological Engineering, Institute of Chemical Processes, Seoul National University, Seoul 08826, Republic of Korea. [5]Center for Humanoid Research, Artificial Intelligence and Robotics Institute, Korea Institute of Science and Technology (KIST), Seoul 02792, Republic of Korea. [6]Soft Hybrid Materials Research Center, Advanced Materials Research Division, Korea Institute of Science and Technology (KIST), Seoul 02792, Republic of Korea. [7]Division of Nano and Information Technology, University of Science and Technology of Korea, Daejeon 34113, Republic of Korea. [8]Department of Materials Science and Engineering, YU-KIST Institute, Yonsei University, Seoul 03722 Republic of Korea.
*Corresponding author. Email: cschoi91@kist.re.kr (C.C.); dkim98@snu.ac.kr (D.-H.K.); mkchoi@unist.ac.kr (M.K.C.)
†These authors contributed equally to this work.

extraction. This adjustable feature of the phototransistor is inspired by dopamine-mediated neuronal excitability regulation of human synapses (*37*), where dopamine influences the excitatory postsynaptic potential (EPSP) accumulation amplitude via excitatory or inhibitory interactions with dopamine receptors (*38*–*40*). This regulatory mechanism is emulated by using a synaptic phototransistor with multi-gating effects, i.e., electrostatic gating effect by a gate-applied bias coupled with photogating effect by interfacial hole trapping. Specifically, the electrostatic gating effect either facilitates or inhibits the time-dependent photocurrent generation induced by photogating effect, modulating the photocurrent accumulation amplitude. With such features, the adjustable synaptic phototransistors can enhance details of both bright and dim regions in target images via inhibitory and excitatory modes of in-sensor multilevel image adjustment, respectively, enabling high-clarity contour extraction under various lighting conditions. Upon the simulation with DeepLab v3+ model (*41*) using Cambridge-driving Labeled Video Database (CamVid) (*42*), contours of road images can be extracted with high-level clarity through in-sensor processing, facilitating precise semantic segmentation with a global accuracy of ~86.7% as well as improving data transmission efficiency with a compression ratio of ~91.8%.

RESULTS

In-sensor multilevel image adjustment for high-clarity contour extraction

The adjustable feature of the phototransistor is inspired by dopamine-mediated neuronal excitability regulation of human synapses. In human synapses, signal transmission between neurons begins with the release of excitatory neurotransmitters (e.g., glutamate), triggered by the arrival of presynaptic action potentials (APs) (Fig. 1A, left) (*43*). These neurotransmitters bind glutamate receptors on postsynaptic neurons to generate EPSP. As consecutive presynaptic APs arrive, EPSPs accumulate across dendrites. Synaptic photodetectors have been developed by emulating these glutamatergic responses (fig. S2, A to C), aiming at contrast enhancement through in-sensor processing (*28*, *30*, *35*). However, the amplitude of photocurrent accumulation in traditional synaptic photodetectors is fixed as a specific value, which often cannot be optimal under uneven and dynamic light conditions encountered in various robotic vision scenarios (*44*). To ensure consistently high quality of the robot vision regardless of fluctuations in the lighting condition, both brightness and contrast of the vision system should be elaborately adjusted.

In the case of synapse, the EPSP accumulation amplitude is regulated by the interaction of dopamine with dopamine receptors on postsynaptic neurons such as excitatory D1-like receptors or inhibitory D2-like receptors, referred to as dopaminergic responses (Fig. 1A, right, and fig. S2D) (*37*). Specifically, activation of D1-like receptors phosphorylates glutamate receptors and promotes their expression on the cell surface, thereby facilitating neuronal excitability and increasing the EPSP amplitude [fig. S2E (i)] (*38*, *45*). In contrast, activation of D2-like receptors leads to a reduced expression of glutamate receptors on the cell surface and the closure of ion channels, inhibiting neuronal excitability for glutamatergic responses and decreasing the EPSP amplitude [fig. S2E (ii)]. See text S1 for details of EPSP accumulation features coupled with dopamine-mediated neuronal excitability regulation.

Inspired by this mechanism of dopamine-mediated neuronal excitability regulation, we fabricate the adjustable synaptic phototransistor, whose photocurrent accumulation amplitude is regulated by the electrostatic gating bias (V_{el}). More details about the device fabrication are provided in Materials and Methods and fig. S3. Please note that our synaptic phototransistor exhibits time-dependent photocurrent generation due to photogating effect induced by interfacial hole trapping (V_{ph}) at the MoS_2 channel (Fig. 1B, left) (*32*). V_{el} modulates the photocurrent generation amount and, thus, either facilitates or inhibits the photocurrent accumulation, analogous to how dopamine receptors provide excitatory or inhibitory pathways, respectively (Fig. 1B, right).

For example, with a low V_{el} (inhibitory mode), the photocurrent accumulation amplitude can be suppressed. Consequently, an adequate light dose, both in terms of duration and intensity, is necessary to accumulate the photocurrent above the activation threshold (i.e., a point where the photocurrent becomes distinguishable from dark current) [fig. S2F (ii)]. This leads to selective filtering of dim regions (i.e., regions with insufficient light dose), leaving only the bright regions [Fig. 1C (i)]. On the other hand, a high V_{el} (excitatory mode) amplifies the photocurrent accumulation amplitude [fig. S2F (i)], intensifying dim objects while causing bright objects to saturate [Fig. 1C (ii)]. This results in another image, where the visibility of dim regions can be enhanced. Through either inhibitory or excitatory mode, therefore, the adjustable synaptic phototransistors can extract two distinct images from a single scene: one highlights bright regions and the other highlights dim regions (Fig. 1C).

The photocurrent accumulation characteristics can be tailored even more finely according to various lighting conditions by modulating V_{el} as more discrete values, which enables image adjustment by multiple levels via in-sensor processing. This in-sensor multilevel image adjustment ensures the acquisition of clear images with optimal brightness and contrast across regardless of dim or bright regions. This feature is particularly effective in varying lighting scenarios, from intense bright condition of sunny days to subdued light condition of cloudy days. For sunny days, an image acquired with V_{el} of −5 V selectively enhances visibility in bright regions by filtering out dimmer areas (Fig. 1D, red box). Conversely, V_{el} of −1 V selectively accentuates dim regions by saturating overly bright regions, visualizing shadowed or less-illuminated areas clearly (Fig. 1D, blue box). For cloudy days, relatively higher V_{el} (e.g., 1 V for bright regions and 2 V for dim regions) can be applied to counterbalance low-intensity surroundings (Fig. 1E), ensuring balanced image capture despite environmental light condition changes. See fig. S4 for the proposed workflow of adjustable synaptic phototransistors.

Two in-sensor–adjusted images, each emphasizing either bright or dim regions, can be used to achieve high-clarity contour extraction (Fig. 2A). First, each image is binarized using the adaptive thresholding method, producing two contour-extracted images that highlight details in bright and dim regions, respectively. These contour-extracted images are then merged using AND logic operation, creating a high-clarity contour-extracted image that incorporates details from both bright and dim regions (Fig. 2A, middle). Please note that conventional image processing methods often yield low-clarity contours that deep neural networks can struggle to interpret [see incorrect pixel classification in Fig. 2B (i)]. These methods, thus, require additional data processing steps for image adjustment, which lead to increased power consumption and data latency. In contrast, our in-sensor processing method not only streamlines the image processing workflow but also achieves high-clarity contour extraction, thereby enhancing both accuracy and efficiency of semantic segmentation [Fig. 2B, (ii), and fig. S1B]. See movies S1 and S2 to

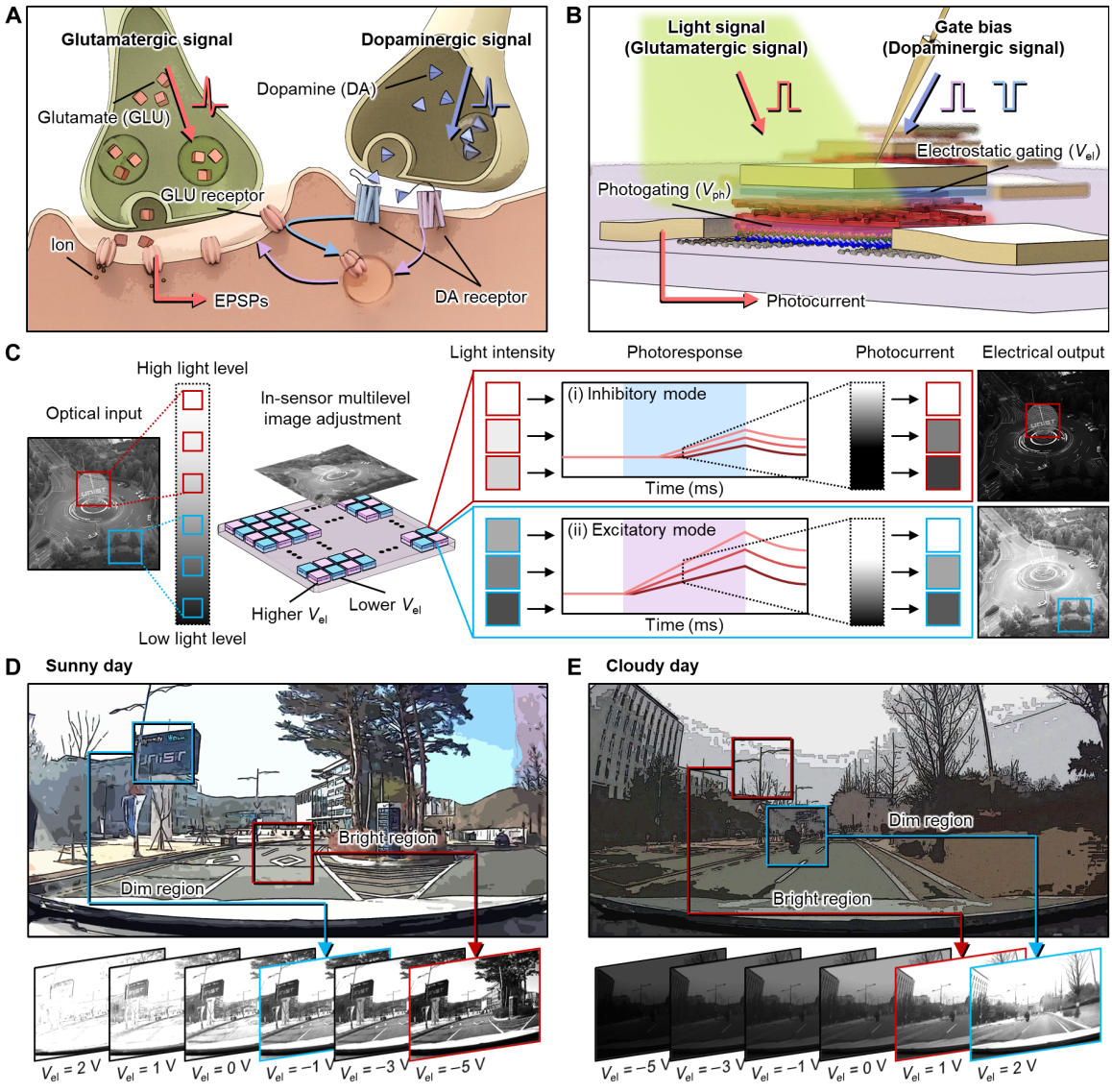

Fig. 1. In-sensor multilevel image adjustment enabled by adjustable synaptic phototransistors. (**A**) Schematic illustration of biological synapses showing glutamatergic response for EPSP accumulation and its dopaminergic regulation. (**B**) Schematic illustration of adjustable synaptic phototransistors with light-induced photogating effect for photocurrent accumulation and gate bias-driven electrostatic gating effect for photocurrent regulation. (**C**) Schematic showing in-sensor multilevel image adjustment capabilities of adjustable synaptic phototransistors. Images highlighting either bright or dim regions are selectively captured through inhibitory (top) and excitatory (bottom) modes, respectively. It is achieved by nonlinear optoelectronic conversion from optical inputs to electrical outputs, enabled by time-dependent photocurrent accumulation with activation threshold. (**D** and **E**) In-sensor–adjusted images under varying V_{el} (simulations) from real-world road-driving scenarios under sunny (D) and cloudy (E) conditions. Blue and red boxes indicate dim and bright regions, respectively.

compare contour extraction by the proposed method and that by the conventional image processing method under different light conditions, e.g., sunny and cloudy days. The contour extraction results for additional scenarios, including indoor environments and nighttime conditions, are also shown in movies S3 and S4.

Characterization of adjustable synaptic phototransistors

The key attributes enabling the in-sensor multilevel image adjustment are the time-dependent photo-response for photocurrent accumulation and its electrostatic regulation for adjustable functionality. To integrate these attributes within a single device, we fabricate the synaptic phototransistor consisting of a monolayer MoS_2 channel, graphene source/drain electrodes, a poly(1,3,5-trimethyl-1,3,5-trivinyl cyclotrisiloxane) (pV3D3) dielectric, and a Ti/Au gate electrode (Fig. 3, A and B). Despite some light loss caused by the top gate electrode (fig. S5), this device structure is effective in achieving time-dependent photo-response due to the abundant interfacial charge traps at the MoS_2-pV3D3 heterostructure (*32*). Furthermore, this device ensures long-term stability over time and demonstrate durability through repeated measurements (fig. S6).

In this device architecture, conductivity of the MoS_2 channel is affected by multi-gating effects: (i) photogating effect by hole

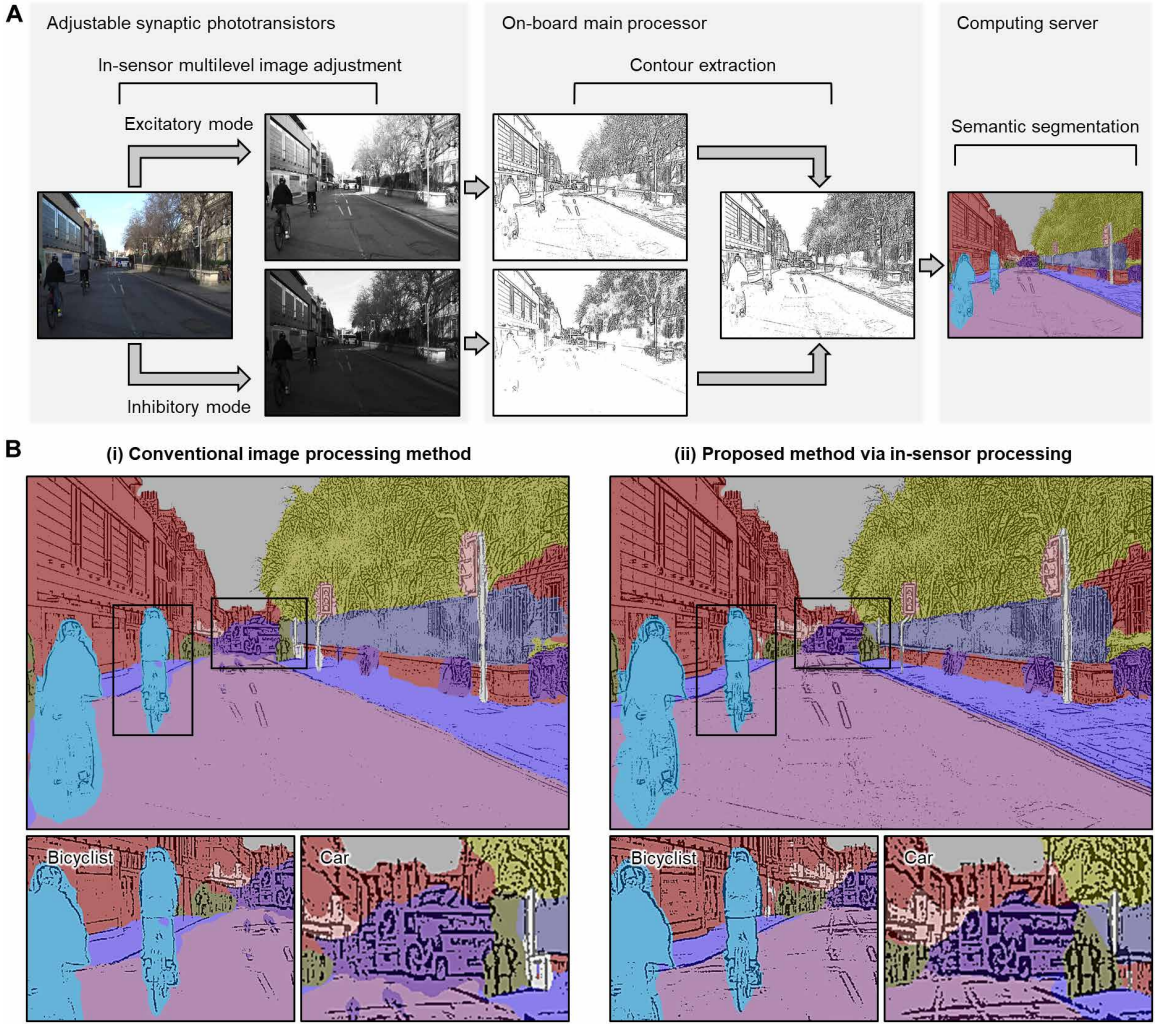

Fig. 2. High-clarity semantic segmentation enabled by in-sensor multilevel image adjustment. (**A**) Schematic illustration showing semantic segmentation workflow based on adjustable synaptic phototransistors. Contours in the two in-sensor–adjusted images, each of which highlights dim (top) and bright (bottom) regions through excitatory and inhibitory modes, respectively, are extracted and merged to produce a high-clarity contour-extracted image that neural networks accurately recognize. (**B**) Comparative semantic segmentation results of a road-driving image for conventional image processing method (left) and our proposed in-sensor processing method (simulation) (right). The colored overlays represent areas recognized as distinct objects by DeepLab v3+ model, showing high-clarity contour extraction and high-accuracy semantic segmentation achieved through in-sensor multilevel image adjustment.

trapping at the MoS_2-pV3D3 heterointerface and (ii) electrostatic gating effect by electron accumulation at the gate electrode (Fig. 3C). Both effects generate localized electrical fields that modulate Fermi level of the MoS_2 channel (fig. S7), thereby altering the channel conductivity (*46*, *47*). The detailed mechanisms of the Fermi level modulation by the multi-gating effects are described in text S2.

The photogating effect results in time-dependent photocurrent accumulation due to the slow dynamics of interfacial hole trapping (*32*). Also, the probability of interfacial hole trapping and, thus, the extent of photogating depend on the light dose, defined as the product of light intensity and light irradiation duration; higher light dose results in larger photocurrent accumulation. Additionally, electrostatic gating effect, controlled by V_{el}, finely regulates the photocurrent accumulation characteristics by introducing additional electric fields that offset the photogating effect. More negative V_{el} requires greater photogating effect to accumulate a specific photocurrent level, which, in turn, necessitates increased interfacial hole trapping facilitated by higher light dose (Fig. 3D) (*47*). As a result, under positive V_{el}, low light dose is sufficient to accumulate the desired photocurrent, whereas more negative V_{el} demands higher light dose to reach the same current level.

Consequently, our device exhibits V_{el}-dependent activation threshold, i.e., the light dose necessary to generate threshold photocurrent (I_{th}) varies with V_{el} (Fig. 3E). We set I_{th} as 0.10 nA to represent the minimal photocurrent distinguishable from the dark current. If the light dose is below the activation threshold, then photocurrent remains negligible. However, once the light dose exceeds this threshold, photocurrent begins to accumulate substantially. Furthermore, more negative V_{el} increases the light dose required to reach the activation threshold.

For instance, under low light dose conditions (e.g., light exposure with intensity of 0.70 mW cm^{-2} and duration of 220 ms), which

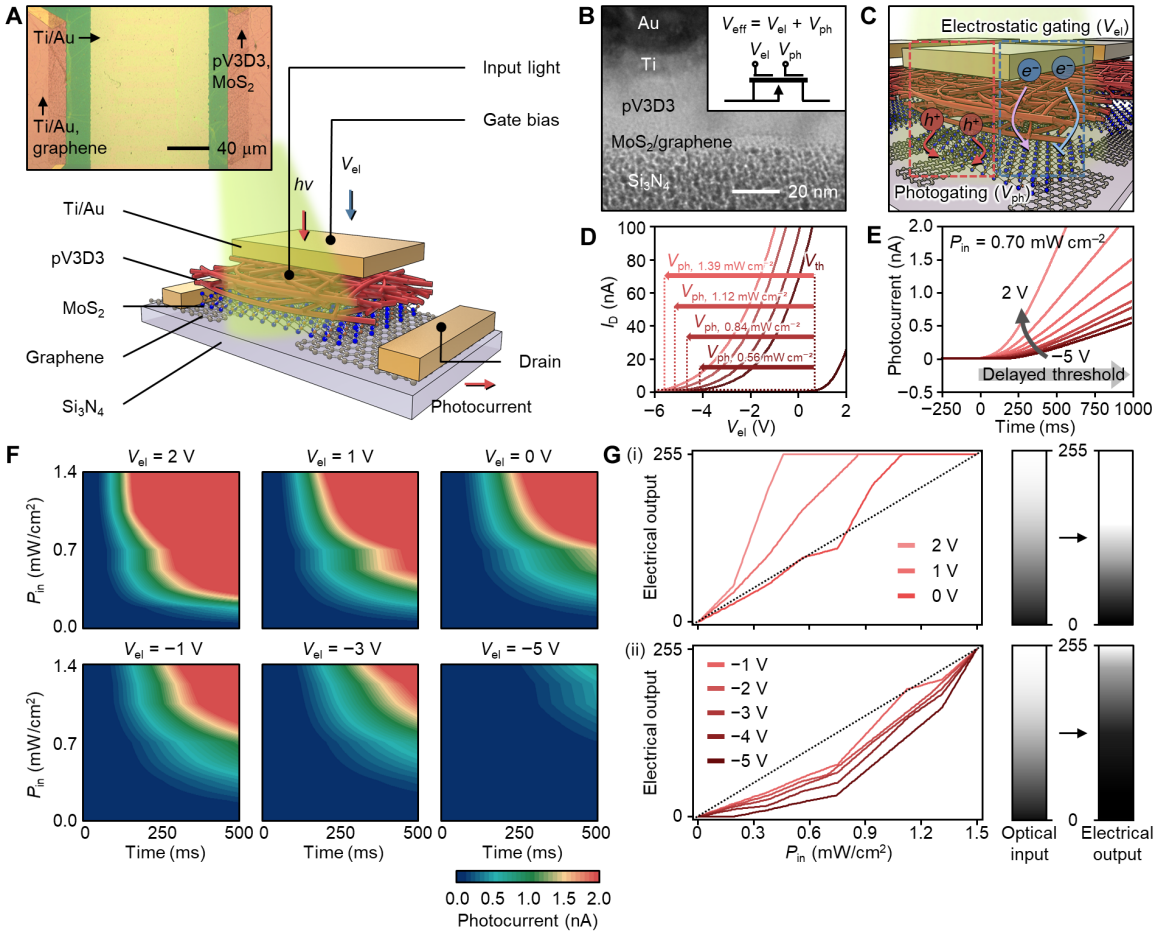

Fig. 3. Characterization of adjustable synaptic phototransistors. (**A** and **B**) Schematic illustration (A) and cross-sectional transmission electron microscopy image (B) of the adjustable synaptic phototransistor. Inset shows its optical microscope image. (**C**) Schematic illustration showing photogating effect induced by interfacial hole trapping and electrostatic gating effect induced by gate electron accumulation, both modulating conductivity of MoS_2 channel. (**D**) Transfer curves of the adjustable synaptic phototransistor under different light intensities. (**E**) Time-dependent photocurrent accumulation characteristics under different V_{el}, ranging from −5 to 2 V, at light intensity of 0.70 mW cm^{-2}. (**F**) The photocurrent accumulation amplitudes as a function of light intensity (P_{in}) and exposure duration under different V_{el}. (**G**) Nonlinear optoelectronic conversion of adjustable synaptic phototransistor depending on V_{el}, converting light intensities (left) into photocurrents (right). Photocurrent measurements are conducted at 250 ms across light intensities from 0 to 1.39 mW cm^{-2}. The photocurrents are normalized to the maximum values measured at the highest light intensity for each V_{el}, but, for positive V_{el} (from 0 to 2 V), the maximum value measured at V_{el} of −1 V is used to induce saturation from bright inputs.

are insufficient to reach the activation threshold, photocurrent less than I_{th} is generated with V_{el} of −5 V (Fig. 3E). However, once this threshold is surpassed by increasing light intensity or extending exposure duration, the photocurrent exceeds I_{th} and increases (fig. S8). Meanwhile, applying more positive V_{el} allows the photocurrent to reach I_{th} with lower light dose. Specifically, Fig. 3F presents how accumulated photocurrents vary according to light intensity and exposure duration, dependent on V_{el}. The dark blue areas represent light doses below the threshold, where the accumulated photocurrent is less than I_{th}. As V_{el} decreases from 2 to −5 V, the dark blue areas expand, indicating that a higher light dose is required to compensate for the V_{el} reduction. In addition, the adjustable synaptic phototransistor exhibit V_{el}-dependent activation threshold upon the pulsed light irradiation, indicative of synaptic plasticity–like photo-responses (fig. S9).

Therefore, by adjusting V_{el}, we can control the activation threshold, thereby regulating photocurrent accumulation characteristics, characterized by linearity coefficient (α; $I_{ph} = P_{in}^{\alpha}$) (Fig. 3G). These features enable our synaptic phototransistor to perform nonlinear optoelectronic conversion, transforming light intensities (optical inputs) into tailored photocurrents (electrical outputs) to suit various light conditions. Specifically, with positive V_{el} (e.g., 0, 1, and 2 V), α is below 1, amplifying photocurrents from dim optical inputs, saturating those from bright ones, and thereby enhancing contrast in low-light conditions [Fig. 3G (i)]. In contrast, negative V_{el} (from −1 to −5 V) increases α above 1, suppressing photocurrents from dim optical inputs, amplifying those from bright ones, and thus increasing contrast in bright regions [Fig. 3G (ii)]. This V_{el}-dependent nonlinear optoelectronic conversion enables multilevel adjustment of pixel intensity through in-sensor processing (fig. S10), allowing our device to capture two distinct images: one accentuating bright regions and the other highlighting dim regions.

Evaluation of in-sensor multilevel image adjustment

For evaluation of in-sensor multilevel image adjustment capabilities, we fabricate a 3 × 3 array of adjustable synaptic phototransistors and

characterize it under varying lighting conditions (fig. S11). The irradiated light patterns are designed to simulate bright and dim regions in sunny (Fig. 4A, left) and cloudy (Fig. 4B, left) days. These patterns are calibrated in grayscale, ranging from 0 (dark) to 255 (intensity of 1.39 mW cm^{-2}). Photocurrents from each pixel are measured at an exposure time of 250 ms under various V_{el} settings, tailored to either inhibitory or excitatory modes for each lighting scenario (Fig. 4, A and B, middle and right). The photocurrent accumulation characteristics are shown in fig. S12.

To quantitatively assess contrast enhancement, we characterize image contrast (C), defined as a difference of averaged grayscale values (G) between pattern-irradiated areas and background areas ($C = G_{pattern} - G_{background}$) (*4*). Initially, two light patterns are prepared for sunny days: One simulates bright regions ("n" pattern) and the other simulates dim regions ("v" pattern), each exhibiting an image contrast of 102 (Fig. 4A, left). Under inhibitory modes ($V_{el} = -4$ V), the n pattern captured by adjustable synaptic phototransistors exhibits an enhanced image contrast of 168.5, while the v pattern shows a lower contrast enhancement ($C = 73.3$) (Fig. 4, A, middle, and C, top). This indicates that the inhibitory mode effectively enhances visibility in bright regions but is less effective for visibility enhancement in dim regions. Instead, the excitatory mode ($V_{el} = -1$ V) yields contrast enhancement ($C = 109.5$) for v pattern (Fig. 4, A, right, and C, top), enhancing visibility in dim regions. As such, high-contrast images for either bright or dim patterns can be captured through either inhibitory or excitatory modes, respectively.

For cloudy days, higher V_{el} is used to compensate for lower light intensities. Also, in this case, image contrast for bright and dim patterns can be enhanced by applying V_{el} of 1 and 2 V, targeting inhibitory and excitatory modes, respectively (Fig. 4B, middle and right). For example, the image contrast of the n pattern improves from 102 to 176.8 under an inhibitory mode and that of the v pattern from 51 to 137.1 under an excitatory mode (Fig. 4C, bottom).

The efficacy of the in-sensor multilevel image adjustment is also validated through simulations using the device parameters (Fig. 3G). Simulations are applied to driving road images under two distinct lighting scenarios: sunny day (intense lighting conditions; Fig. 4D, left) and cloudy day (subdued lighting conditions; Fig. 4E, left).

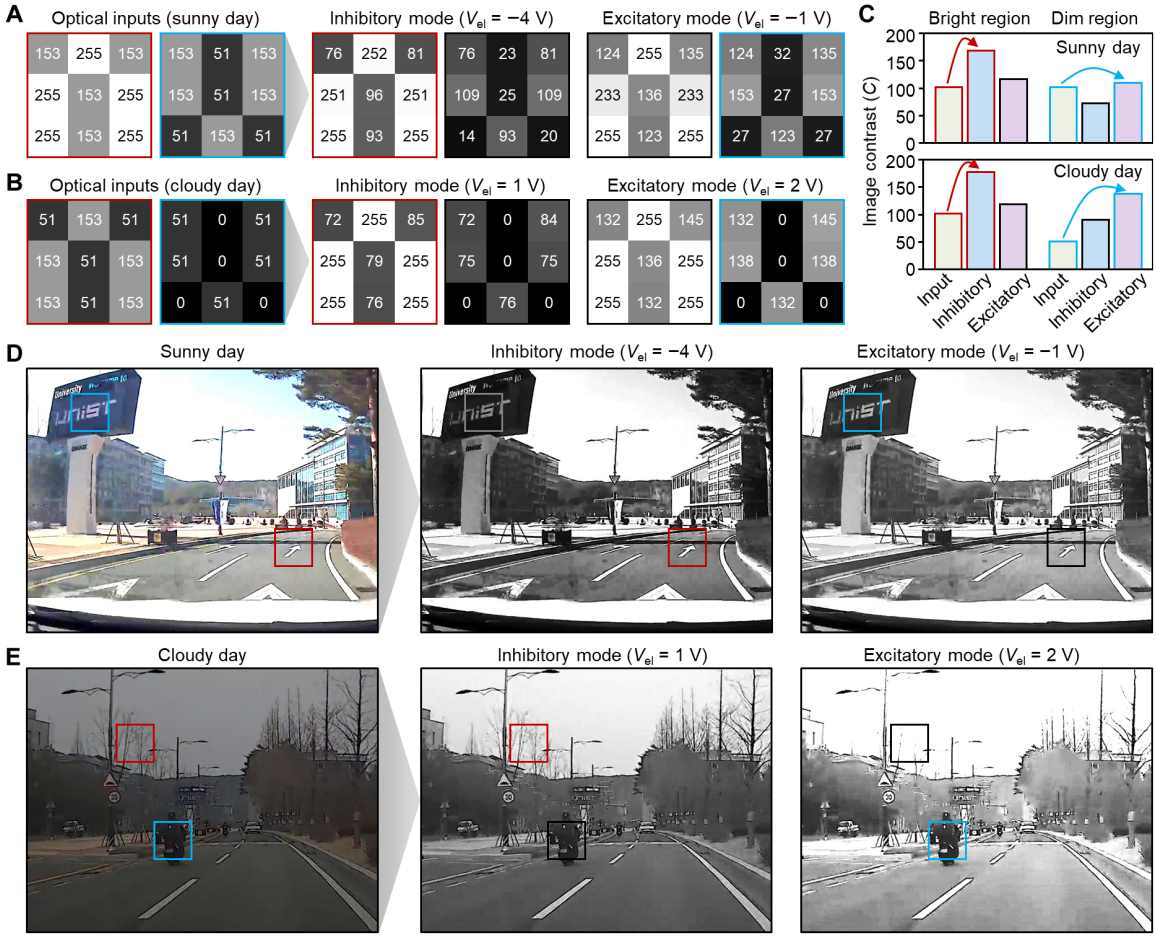

Fig. 4. Evaluation on in-sensor multilevel image adjustment. (**A** and **B**) Normalized photocurrents measured by 3 × 3 array of adjustable synaptic phototransistors under patterned light irradiation of bright n pattern and dim v pattern on sunny (A) and cloudy (B) days (left). Photocurrents are measured under inhibitory (middle) and excitatory (right) modes, applying V_{el} of −4 and −1 V for sunny days, and V_{el} of 1 and 2 V for cloudy days, respectively. (**C**) Image contrast (C) comparison of in-sensor–adjusted images by inhibitory and excitatory modes, tailored for sunny (top) and (bottom) days. (**D** and **E**) Road-driving raw images (left) and in-sensor–adjusted images (simulations) through inhibitory (middle) and excitatory (right) modes of adjustable synaptic phototransistors, on sunny (D) and cloudy (E) days. Compared to the raw images, bright and dim regions are accentuated by inhibitory and excitatory modes, highlighted by red and blue boxes, respectively.

With the inhibitory mode (V_{el} of −4 V for sunny days and 1 V for cloudy days), visibility in bright regions is selectively enhanced by increasing the image contrast in these areas while dimming the shadowed or dark regions (Fig. 4, D and E, middle). Conversely, with the excitatory mode (V_{el} of −1 V for sunny days and 2 V for cloudy days), visibility of objects within dim regions is enhanced by increasing the image contrast there while saturating the bright regions (Fig. 4, D and E, right). With such a dual-mode operation, the visibility of all bright and dim objects can be optimized, highlighted from the background (red and blue boxes in Fig. 4, D and E) and ensuring balanced perception across diverse lighting conditions. Please see table S1 for detailed comparisons of the adjustable synaptic phototransistor with previous relevant works.

Evaluation on high-clarity contour extraction

Contour extraction refers to computational vision processing techniques used for data compaction, which visualizes essential object contours and removes unnecessary backgrounds by isolating relevant characteristics based on color, intensity, and texture, ensuring accurate object detection as well as efficient data transmission (text S3 for details). To achieve high-clarity contour extraction, brightness and contrast of image data should be optimal. However, additional software-based image processing steps for adjusting brightness and contrast imposes computational demands to onboard processors.

In-sensor multilevel image adjustment using adjustable synaptic phototransistors, which enhances visibility in either dim or bright regions, enables high-clarity contour extraction without additional computational image adjustments. For qualitative clarity evaluation, we compare contour extraction results from in-sensor–adjusted images to those from raw images and software-adjusted images. Figure 5A shows the original high-resolution images before contour extraction. Without any adjustments (neither software nor hardware approaches), contours of the objects (e.g., traffic signs) appear blurred and noisy (Fig. 5B). This issue can be addressed through software-based image adjustment (e.g., contrast enhancement) (Fig. 5C), but at the cost of power consumption and data latency burdening onboard processors. Furthermore, contours of dark objects (e.g., trees) still remains indistinct. In contrast, the contour extraction results from in-sensor–adjusted images exhibit clear distinctions across all objects despite the absence of additional image adjustment steps (Fig. 5D). Another contour extraction technique, edge-detection method using Sobel operator, shows similar high-clarity results for in-sensor–adjusted images (fig. S13), validating that the in-sensor multilevel image adjustment is effective for contour extraction, regardless of the specific method used.

The high-clarity contour extraction enabled by adjustable synaptic phototransistor is also quantitatively validated using artificial intelligence (AI)-based evaluation methodology; the high clarity of contour-extracted images results in high recognition accuracy by AI models. Specifically, we perform convolutional neural network–based semantic segmentation test with DeepLab v3+ model and road-driving dataset (CamVid) (Fig. 5E) (*48*). The CamVid comprises 701 road-driving images captured under various lighting scenarios, including both sunny and cloudy days. To optimize object detection performance, we adjust brightness and contrast of training images to balance pixel intensities across the dataset, and 40% contrast enhancement yields the highest accuracy (table S2). See text S4 and fig. S14 for details of training image adjustment.

We then compare pixel accuracy and intersection-over-union (IoU) metrics using the datasets of contour-extracted images, obtained from raw images, software-adjusted images (with 40% contrast enhancement), and in-sensor–adjusted images, via adaptive thresholding method (Fig. 5F, fig. S15, and table S3). The in-sensor–adjusted images allow enhanced semantic segmentation results in comparison to raw images, where global accuracy increases from 83.2 to 86.7%, and weighted IoU increases from 0.73 to 0.79. Although software-based image adjustment yields higher metrics (global accuracy of 87.8% and weighted IoU of 0.81), it relies on additional processing for adjusting image brightness and contrast, resulting in larger power consumption and longer processing time than our approach.

In addition, we validate that object detection through high-clarity contour extraction can achieve high-accuracy while compressing data volume, compared to traditional approaches using raw road images (i.e., high-resolution images) (fig. S16). Despite substantial data compression ratio of 91.8%, achieved through contour extraction and data binarization, semantic segmentation achieved by our devices demonstrates pixel accuracy and IoU metrics comparable to traditional methods (Fig. 5, G and H). The data compression ratio was calculated by comparing the data size of CamVid (~560 MB) with its contour-extracted counterparts (~45.8 MB).

DISCUSSION

We develop the in-sensor multilevel image adjustment method using adjustable synaptic phototransistors for high-clarity contour extraction. This device is inspired from dopamine-mediated neuronal excitability regulation mechanisms, using time-dependent photocurrent accumulation enabled by photogating effect and its electrostatic regulation by modulating gating bias. These features lead to nonlinear optoelectronic conversion from optical inputs to electrical outputs, where the linearity coefficient can be adjusted via V_{el} control. Consequently, the adjustable synaptic phototransistor can perform in-sensor multilevel image adjustment, capturing well-defined images with optimal brightness and contrast under diverse lighting conditions. The clarity of extracted contours from these images is validated both qualitatively and quantitatively, resulting in enhancements in object detection performance in terms of data compaction and accuracy.

Nevertheless, breakthroughs are still required to enable the practical application of adjustable synaptic phototransistors. To this end, it is essential to achieve a scalable array of adjustable synaptic phototransistors. This requires device-to-device uniformity, which necessitates advancements in fabrication techniques, such as uniform synthesis of high-quality MoS_2 monolayers and uniform formation of the MoS_2-pV3D3 heterostructure (*49*, *50*). Additionally, active-matrix array designs should be implemented to minimize the external wiring complexity as the array size scales up, ensuring stable and high-quality signal acquisition. Despite these challenges, our proposed method via in-sensor processing has high potential to optimize data transmission efficiency without compromising accuracy, paving the way for advanced vision processing techniques particularly for energy-efficient and high-performance robotic vision applications.

MATERIALS AND METHODS

Preparation of the graphene and MoS_2 film

Graphene was purchased from Graphene Square. A monolayer MoS_2 film was synthesized via atmospheric pressure chemical vapor deposition process (*51*). Initially, a 2-inch (5.08-cm) sapphire wafer was cleaned through sonication in acetone and ethanol for 10 min, followed

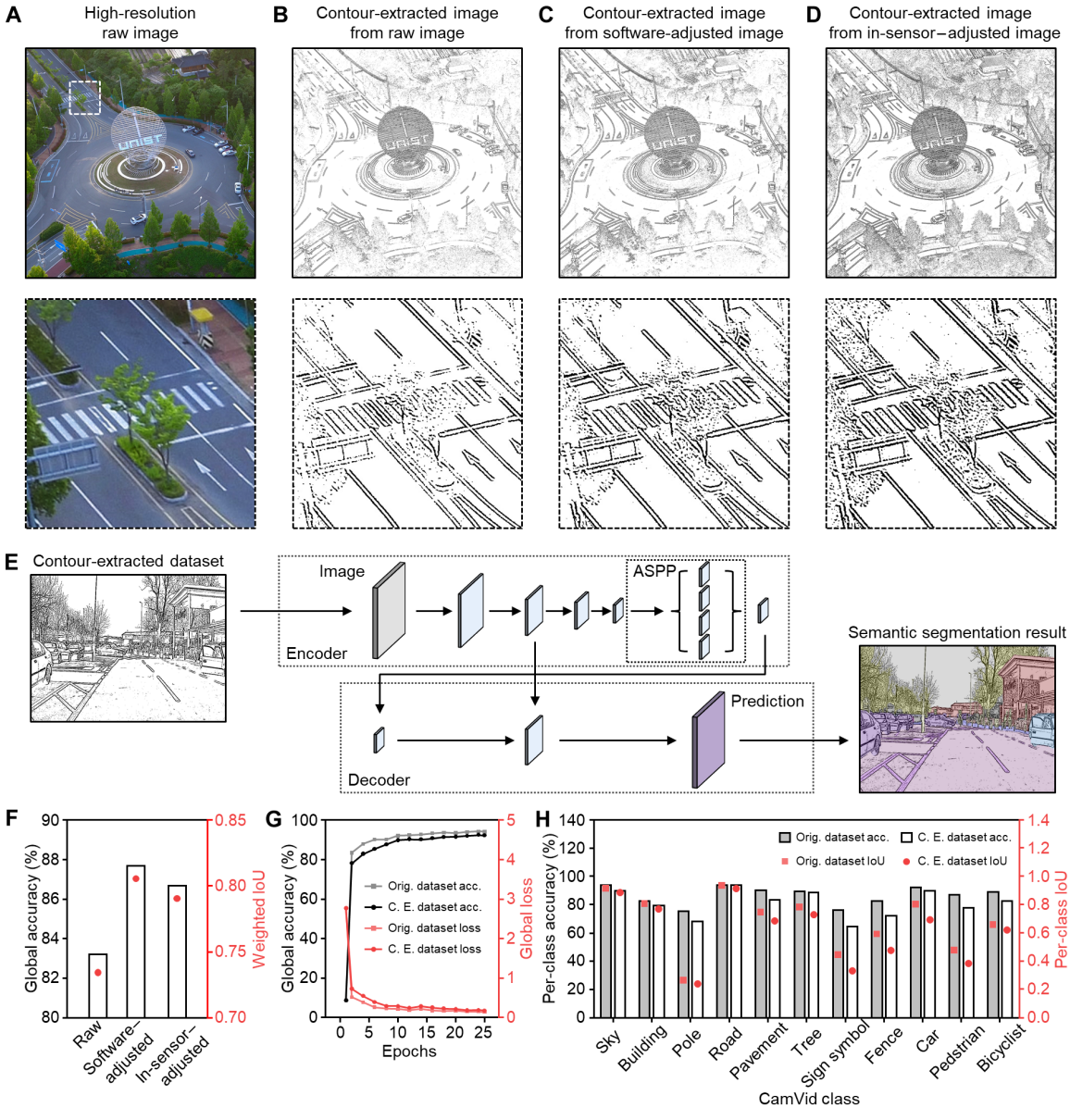

Fig. 5. Evaluation on high-clarity contour extraction. (**A** to **D**) High-resolution images (i.e., raw images) (A) of roundabout (top) and crosswalk (bottom) and contour-extracted images via adaptive thresholding method from raw images (B), software-based adjusted images (40% contrast enhancement) (C), and in-sensor–adjusted images (simulation) (D). (**E**) Schematic showing the architecture of DeepLab v3+ model for semantic segmentation test on contour-extracted dataset of road images. (**F**) Global accuracy and weighted intersection-over-union (IoU) metrics across contour-extracted datasets obtained from raw images, software-adjusted images, and in-sensor–adjusted images. (**G**) Global accuracy and loss of semantic segmentation test over training epochs for original (i.e., high-resolution) and contour-extracted (C. E.) dataset. (**H**) Per-class accuracy and IoU across original and contour-extracted (C. E.) dataset. ASPP, Atrous Spatial Pyramid Pooling.

by rinse in isopropyl alcohol. The cleaned substrate was loaded into a muffle furnace, ramped to 1000°C for 2 hours, annealed at 1000°C for 2 hours, and cooled down to room temperature under with nitrogen gas purge. Subsequently, a precursor solution of NaCl-MoO_2 was spin coated onto the sapphire substrate. Monodisperse MoO_2 nanoparticles were prepared via colloidal synthesis, and methanol solution containing NaCl (0.1 M) was added to the MoO_2 solution at volume ratio of 1:50. A crucible containing sulfur powder (15 mg) and the spin-coated sapphire substrate were loaded into two separate furnaces, heated at 150° and 650°C, respectively, under argon flow of 500 standard cubic centimeters per minute. After growth period of 30 min, furnaces were opened and cooled down to room temperature.

Fabrication and characterization of the adjustable synaptic phototransistor

The fabrication process of the adjustable synaptic phototransistor began with the transfer of graphene film (~2 nm) onto Si_3N_4 layer (50 nm), deposited on a Si wafer. Ti/Au electrodes (5/25 nm) were deposited and patterned using liftoff process, and the graphene was patterned as interdigitated source/drain electrodes with a channel

length of 10 μm by photolithography and dry etching. The monolayer MoS_2 film was transferred onto the graphene electrodes and patterned by photolithography and dry etching. A pV3D3 dielectric (30 nm) was deposited using initiated chemical vapor deposition and patterned by photolithography and dry etching. Last, Ti/Au gate electrodes (5/25 nm) were deposited by thermal evaporation and patterned using liftoff process.

A cross-sectional image of adjustable synaptic phototransistor was captured using Cs corrected transmission electron microscope (JEM-ARM200F, JEOL, Japan). The transmittance of top gate structure was measured using an ultraviolet–visible–near-infrared spectrophotometer (Lambda 750, PerkinElmer). Fermi level of MoS_2-pV3D3 heterostructure under various V_{el} was analyzed using Kelvin probe force microscopy (XE 100, Park Systems, Korea). Transfer curves of adjustable synaptic phototransistors were characterized using a parameter analyzer (B1500A, Agilent, USA). Photocurrent measurements for analyzing time-dependent photo-response were performed using a multichannel analog-to-digital converter after converting the photocurrent into the voltage signal with a preamplifier (SR570, Stanford Research Systems, USA) (fig. S11). A commercial green light-emitting diode (peak emission wavelength of 520 nm) was used as light source, and its intensity and exposure duration were controlled using an Arduino Uno board.

Simulation using empirical parameters of adjustable synaptic phototransistor

To validate the feasibility of in-sensor multilevel image adjustment for high-clarity contour extraction, simulations were conducted to emulate the in-sensor–adjusted images using empirical parameters derived from V_{el}-dependent nonlinear optoelectronic conversion of the adjustable synaptic phototransistor. The accumulated photocurrents of adjustable synaptic phototransistor were measured under varying light intensities, exposure durations, V_{el} (fig. S8). Based on these measurement results, a lookup table of normalized photocurrent values at exposure duration of 250 ms was created through interpolation (Fig. 3G).

The simulation process involved converting the light intensities of high-resolution raw images into corresponding values from the lookup table based on specific V_{el}, thereby generating in-sensor–adjusted images. The V_{el} values of excitatory and inhibitory modes were selected according to the lighting conditions. Subsequently, contours were extracted from the in-sensor–adjusted images, and the contour-extracted images for both modes were merged using logic operations to generate a high-clarity contour-extracted image. All relevant source codes are included in the Supplementary Materials.

Supplementary Materials

The PDF file includes:

Text S1 to S4
Figs. S1 to S18
Tables S1 to S3
Legends for movies S1 to S4
References

Other Supplementary Material for this manuscript includes the following:

Movies S1 to S4

REFERENCES AND NOTES

1. Y. M. Song, Y. Xie, V. Malyarchuk, J. Xiao, I. Jung, K.-J. Choi, Z. Liu, H. Park, C. Lu, R.-H. Kim, R. Li, K. B. Crozier, Y. Huang, J. A. Rogers, Digital cameras with designs inspired by the arthropod eye. *Nature* **497**, 95–99 (2013).
2. L. Gu, S. Poddar, Y. Lin, Z. Long, D. Zhang, Q. Zhang, L. Shu, X. Qiu, M. Kam, A. Javey, Z. Fan, A biomimetic eye with a hemispherical perovskite nanowire array retina. *Nature* **581**, 278–282 (2020).
3. Z. Long, X. Qiu, C. L. J. Chan, Z. Sun, Z. Yuan, S. Poddar, Y. Zhang, Y. Ding, L. Gu, Y. Zhou, W. Tang, A. K. Srivastava, C. Yu, X. Zou, G. Shen, Z. Fan, A neuromorphic bionic eye with filter-free color vision using hemispherical perovskite nanowire array retina. *Nat. Commun.* **14**, 1972 (2023).
4. F. Liao, Z. Zhou, B. J. Kim, J. Chen, J. Wang, T. Wan, Y. Zhou, A. T. Hoang, C. Wang, J. Kang, J.-H. Ahn, Y. Chai, Bioinspired in-sensor visual adaptation for accurate perception. *Nat. Electron.* **5**, 84–91 (2022).
5. M. Kim, S. Chang, M. Kim, J.-E. Yeo, M. S. Kim, G. J. Lee, D.-H. Kim, Y. M. Song, Cuttlefish eye–inspired artificial vision for high-quality imaging under uneven illumination conditions. *Sci. Robot.* **8**, eade4698 (2023).
6. J. Park, M. S. Kim, J. Kim, S. Chang, M. Lee, G. J. Lee, Y. M. Song, D.-H. Kim, Avian eye–inspired perovskite artificial vision system for foveated and multispectral imaging. *Sci. Robot.* **9**, edk6903 (2024).
7. J. Chen, Z. Zhou, B. J. Kim, Y. Zhou, Z. Wang, T. Wan, J. Yan, J. Kang, J.-H. Ahn, Y. Chai, Optoelectronic graded neurons for bioinspired in-sensor motion perception. *Nat. Nanotechnol.* **18**, 882–888 (2023).
8. L. Mennel, J. Symonowicz, S. Wachter, D. K. Polyushkin, A. J. Molina-Mendoza, T. Mueller, Ultrafast machine vision with 2D material neural network image sensors. *Nature* **579**, 62–66 (2020).
9. W. D. Leon-Salas, S. Balkir, K. Sayood, N. Schemm, M. W. Hoffman, A CMOS imager with focal plane compression using predictive coding. *IEEE J. Solid-State Circuits* **42**, 2555–2572 (2007).
10. K. S. Kim, J. Kwon, H. Ryu, C. Kim, H. Kim, E.-K. Lee, D. Lee, S. Seo, N. M. Han, J. M. Suh, J. Kim, M.-K. Song, S. Lee, M. Seol, J. Kim, The future of two-dimensional semiconductors beyond Moore's law. *Nat. Nanotechnol.* **19**, 895–906 (2024).
11. S. Zhu, T. Xie, Z. Lv, Y.-B. Leng, Y.-Q. Zhang, R. Xu, J. Qin, Y. Zhou, V. A. L. Roy, S.-T. Han, Hierarchies in visual pathway: Functions and inspired artificial vision. *Adv. Mater.* **36**, e2301986 (2024).
12. J. A. Baxter, D. A. Merced, D. J. Costinett, L. M. Tolbert, B. Ozpineci, "Review of electrical architectures and power requirements for automated vehicles" in *Proceedings of the 2018 IEEE Transportation Electrification Conference and Expo (ITEC)* 944–949 (IEEE, 2018), pp. 944–949.
13. T. Li, J. Miao, X. Fu, B. Song, B. Cai, X. Ge, X. Zhou, P. Zhou, X. Wang, D. Jariwala, W. Hu, Reconfigurable, non-volatile neuromorphic photovoltaics. *Nat. Nanotechnol.* **18**, 1303–1310 (2023).
14. C. Chen, C. Wang, B. Liu, C. He, L. Cong, S. Wan, Edge intelligence empowered vehicle detection and image segmentation for autonomous vehicles. *IEEE Trans. Intell. Transp. Syst.* **24**, 13023–13034 (2023).
15. Y. Yang, Multi-tier computing networks for intelligent IoT. *Nat. Electron.* **2**, 4–5 (2019).
16. H. Zheng, Q. Liu, I. I. Kravchenko, X. Zhang, Y. Huo, J. G. Valentine, Multichannel meta-imagers for accelerating machine vision. *Nat. Nanotechnol.* **19**, 471–478 (2024).
17. X. Pan, J. Shi, P. Wang, S. Wang, C. Pan, W. Yu, B. Cheng, S.-J. Liang, F. Miao, Parallel perception of visual motion using light-tunable memory matrix. *Sci. Adv.* **9**, eadi4083 (2023).
18. D. Lee, M. Park, Y. Baek, B. Bae, J. Heo, K. Lee, In-sensor image memorization and encoding via optical neurons for bio-stimulus domain reduction toward visual cognitive processing. *Nat. Commun.* **13**, 5223 (2022).
19. S. Song, C. Choi, J. Ahn, J.-J. Lee, J. Jang, B.-S. Yu, J. P. Hong, Y.-S. Ryu, Y.-H. Kim, D. K. Hwang, Artificial optoelectronic synapse based on spatiotemporal irradiation to source-sharing circuitry of synaptic phototransistors. *InfoMat* **6**, e12479 (2024).
20. J. Pang, H. Wu, H. Li, T. Jin, J. Tang, G. Niu, Reconfigurable perovskite X-ray detector for intelligent imaging. *Nat. Commun.* **15**, 1769 (2024).
21. T. Wang, M. M. Sohoni, L. G. Wright, M. M. Stein, S.-Y. Ma, T. Onodera, M. G. Anderson, P. L. McMahon, Image sensing with multilayer, nonlinear optical neural networks. *Nat. Photon.* **17**, 408–415 (2023).
22. Y. Wang, Y. Cai, F. Wang, J. Yang, T. Yan, S. Li, Z. Wu, X. Zhan, K. Xu, J. He, Z. Wang, A three-dimensional neuromorphic photosensor array for nonvolatile in-sensor computing. *Nano Lett.* **23**, 4524–4532 (2023).
23. H. Jang, H. Hinton, W.-B. Jung, M.-H. Lee, C. Kim, M. Park, S.-K. Lee, S. Park, D. Ham, In-sensor optoelectronic computing using electrostatically doped silicon. *Nat. Electron.* **5**, 519–525 (2022).
24. P. Arbelaez, M. Maire, C. Fowlkes, J. Malik, Contour detection and hierarchical image segmentation. *IEEE Trans. Pattern Anal. Mach. Intell.* **33**, 898–916 (2010).
25. D. Yang, B. Peng, Z. Al-Huda, A. Malik, D. Zhai, An overview of edge and object contour detection. *Neurocomputing* **488**, 470–493 (2022).
26. S. F. Stefenon, K.-C. Yow, A. Nied, L. H. Meyer, Classification of distribution power grid structures using inception v3 deep neural network. *Electr. Eng.* **104**, 4557–4569 (2022).
27. Y. Yang, C. Pan, Y. Li, X. Yangdong, P. Wang, Z.-A. Li, S. Wang, W. Yu, G. Liu, B. Cheng, Z. Di, S.-J. Liang, F. Miao, In-sensor dynamic computing for intelligent machine vision. *Nat. Electron.* **7**, 225–233 (2024).

28. Y. Deng, S. Liu, X. Ma, S. Guo, B. Zhai, Z. Zhang, M. Li, Y. Yu, W. Hu, H. Yang, Y. Kapitonov, J. Han, J. Wu, Y. Li, T. Zhai, Intrinsic defect-driven synergistic synaptic heterostructures for gate-free neuromorphic phototransistors. *Adv. Mater.* **36**, 2309940 (2024).
29. C. Choi, G. J. Lee, S. Chang, Y. M. Song, D.-H. Kim, Nanomaterial-based artificial vision systems: From bioinspired electronic eyes to in-sensor processing devices. *ACS Nano* **18**, 1241–1256 (2024).
30. F. Zhou, Z. Zhou, J. Chen, T. H. Choy, J. Wang, N. Zhang, Z. Lin, S. Yu, J. Kang, H. P. Wong, Y. Chai, Optoelectronic resistive random access memory for neuromorphic vision sensors. *Nat. Nanotechnol.* **14**, 776–782 (2019).
31. L. Pi, P. Wang, S.-J. Liang, P. Luo, H. Wang, D. Li, Z. Li, P. Chen, X. Zhou, F. Miao, T. Zhai, Broadband convolutional processing using band-alignment-tunable heterostructures. *Nat. Electron.* **5**, 248–254 (2022).
32. C. Choi, J. Leem, M. S. Kim, A. Taqieddin, C. Cho, K. W. Cho, G. J. Lee, H. Seung, H. J. Bae, Y. M. Song, T. Hyeon, N. R. Aluru, S. W. Nam, D.-H. Kim, Curved neuromorphic image sensor array using a MoS_2–organic heterostructure inspired by the human visual recognition system. *Nat. Commun.* **11**, 5934 (2020).
33. H. Seung, C. Choi, D. C. Kim, J. S. Kim, J. H. Kim, J. Kim, S. I. Park, J. A. Lim, J. Yang, M. K. Choi, T. Hyeon, D.-H. Kim, Integration of synaptic phototransistors and quantum dot light-emitting diodes for visualization and recognition of UV patterns. *Sci. Adv.* **8**, eabq3101 (2022).
34. X. Luo, C. Chen, Z. He, M. Wang, K. Pan, X. Dong, Z. Li, B. Liu, Z. Zhang, Y. Wu, C. Ban, R. Chen, D. Zhang, K. Wang, Q. Wang, J. Li, G. Lu, J. Liu, Z. Liu, W. Huang, A bionic self-driven retinomorphic eye with ionogel photosynaptic retina. *Nat. Commun.* **15**, 3086 (2024).
35. L. Shan, R. Yu, Z. Chen, X. Zhang, C. Gao, M. Lian, Y. Hu, T. Guo, H. Chen, Memory-processing-display integrated hardware with all-in-one structure for intelligent image processing. *Adv. Funct. Mater.* **34**, 2315584 (2024).
36. G. Li, D. Xie, H. Zhong, Z. Zhang, X. Fu, Q. Zhou, Q. Li, H. Ni, J. Wang, E.-J. Guo, M. He, C. Wang, G. Yang, K. Jin, C. Ge, Photo-induced non-volatile VO_2 phase transition for neuromorphic ultraviolet sensors. *Nat. Commun.* **13**, 1729 (2022).
37. N. X. Tritsch, B. L. Sabatini, Dopaminergic modulation of synaptic transmission in cortex and striatum. *Neuron* **76**, 33–50 (2012).
38. X. Sun, Y. Zhao, M. E. Wolf, Dopamine receptor stimulation modulates AMPA receptor synaptic insertion in prefrontal cortex neurons. *J. Neurosci.* **25**, 7342–7351 (2005).
39. L. Speranza, U. di Porzio, D. Viggiano, A. de Donato, F. Volpicelli, Dopamine: The neuromodulator of long-term synaptic plasticity, reward and movement control. *Cells* **10**, 735 (2021).
40. T. Wang, M. Wang, J. Wang, L. Yang, X. Ren, G. Song, S. Chen, Y. Yuan, R. Liu, L. Pan, Z. Li, W. R. Leow, Y. Luo, S. Ji, Z. Cui, K. He, F. Zhang, F. Lv, Y. Tian, K. Cai, B. Yang, J. Niu, H. Zou, S. Liu, G. Xu, X. Fan, B. Hu, X. J. Loh, L. Wang, X. Chen, A chemically mediated artificial neuron. *Nat. Electron.* **5**, 586–595 (2022).
41. S. Minaee, Y. Boykov, F. Porikli, A. Plaza, N. Kehtarnavaz, D. Terzopoulos, Image segmentation using deep learning: A survey. *IEEE Trans. Pattern Anal. Mach. Intell.* **44**, 3523–3542 (2021).
42. G. J. Brostow, J. Fauqueur, R. Cipolla, Semantic object classes in video: A high-definition ground truth database. *Pattern Recogn. Lett.* **30**, 88–97 (2009).
43. P. C. Harikesh, C.-Y. Yang, D. Tu, J. Y. Gerasimov, A. M. Dar, A. Armada-Moreira, M. Massetti, R. Kroon, D. Bliman, R. Olsson, E. Stavrinidou, M. Berggren, S. Fabiano, Organic electrochemical neurons and synapses with ion mediated spiking. *Nat. Commun.* **13**, 901 (2022).
44. S. E. Ng, S. K. Vishwanath, J. Yang, S. S. Periyal, A. Nirmal, N. F. Jamaludin, R. A. John, N. Mathews, Advances in multi-terminal transistors as reconfigurable interconnections for neuromorphic sensing and processing. *Adv. Electron. Mater.* **10**, 2300540 (2024).
45. A. Dodda, D. Jayachandran, S. S. Radhakrishnan, A. Pannone, Y. Zhang, N. Trainor, J. M. Redwing, S. Das, Bioinspired and low-power 2D machine vision with adaptive machine learning and forgetting. *ACS Nano* **16**, 20010–20020 (2022).
46. B. Shi, X. Gan, K. Yu, H. Lang, X. Cao, K. Zou, Y. Peng, Electronic friction and tuning on atomically thin MoS_2. *npj 2D Mater. Appl.* **6**, 39 (2022).
47. Z. Yin, H. Li, H. Li, L. Jiang, Y. Shi, Y. Sun, G. Lu, Q. Zhang, X. Chen, H. Zhang, Single-layer MoS_2 phototransistors. *ACS Nano* **6**, 74–80 (2012).
48. C. Yu, J. Wang, C. Peng, C. Gao, G. Yu, N. Sang, "Bisenet: Bilateral segmentation network for real-time semantic segmentation" in *Proceedings of the European Conference on Computer Vision (ECCV)* (Springer, 2018), pp. 325–341.
49. N. Li, Q. Wang, C. Shen, Z. Wei, H. Yu, J. Zhao, X. Lu, G. Wang, C. He, L. Xie, J. Zhu, L. Du, R. Yang, D. Shi, G. Zhang, Large-scale flexible and transparent electronics based on monolayer molybdenum disulfide field-effect transistors. *Nat. Electron.* **3**, 711–717 (2020).
50. H. Moon, H. Seong, W. C. Shin, W.-T. Park, M. Kim, S. Lee, J. H. Bong, Y.-Y. Noh, B. J. Cho, S. Yoo, S. G. Im, Synthesis of ultrathin polymer insulating layers by initiated chemical vapour deposition for low-power soft electronics. *Nat. Mater.* **14**, 628–635 (2015).
51. J. Kim, H. Seung, D. Kang, J. Kim, H. Bae, H. Park, S. Kang, C. Choi, B. K. Choi, J. S. Kim, T. Hyeon, H. Lee, D.-H. Kim, S. Shim, J. Park, Wafer-scale production of transition metal dichalcogenides and alloy monolayers by nanocrystal conversion for large-scale ultrathin flexible electronics. *Nano Lett.* **21**, 9153 (2021).
52. C. Kopp-Scheinpflug, J. R. Steinert, I. D. Forsythe, Modulation and control of synaptic transmission across the MNTB. *Hear. Res.* **279**, 22–31 (2011).
53. G. Csurka, D. Larlus, F. Perronnin, F. Meylan, What is a good evaluation measure for semantic segmentation? in *Proceedings of the British Machine Vision Conference* (British Machine Vision Association, 2013), pp. 1–11.
54. S. Hong, S. H. Choi, J. Park, H. Yoo, J. Y. Oh, E. Hwang, D. H. Yoon, S. Kim, Sensory adaptation and neuromorphic phototransistors based on $CsPb(Br_{1-x}I_x)_3$ perovskite and MoS_2 hybrid structure. *ACS Nano* **14**, 9796–9806 (2020).
55. D. Xie, L. Wei, M. Xie, L. Jiang, J. Yang, J. He, J. Jiang, Photoelectric visual adaptation based on 0D-$CsPbBr_3$-quantum-dots/2D-MoS_2 mixed-dimensional heterojunction transistor. *Adv. Funct. Mater.* **31**, 2010655 (2021).
56. S. M. Kwon, S. W. Cho, M. Kim, J. S. Heo, Y. H. Kim, S. K. Park, Environment-adaptable artificial visual perception behaviors using a light-adjustable optoelectronic neuromorphic device array. *Adv. Mater.* **31**, 1906433 (2019).
57. M. Zhang, Z. Chi, G. Wang, Z. Fan, H. Wu, P. Yang, J. Yang, P. Yan, Z. Sun, An irradiance-adaptable near-infrared vertical heterojunction phototransistor. *Adv. Mater.* **34**, 2205679 (2022).
58. G. Gong, Y. Zhou, Z. Xiong, T. Sun, H. Li, Q. Li, W. Zhao, G. Zhang, Y. Zhai, Z. Lv, H. Tan, Y. Zhou, S.-T. Han, An antagonistic photovoltaic memristor for bioinspired active contrast adaptation. *Adv. Mater.* **36**, 2409844 (2024).
59. L. Li, S. Li, W. Wang, J. Zhang, Y. Sun, Q. Deng, T. Zheng, J. Lu, W. Gao, M. Yang, H. Wang, Y. Pan, X. Liu, Y. Yang, J. Li, N. Huo, Adaptative machine vision with microsecond-level accurate perception beyond human retina. *Nat. Comm.* **15**, 6261 (2024).

Acknowledgments

Funding: This research was supported by IBS-R006-A1 and IBS-R006-D1. This research was also supported by the National Research Foundation of Korea grant funded by the Korean government (MSIT) (RS-2023-00209466, 2022R1A5A6000846); by the Korea Evaluation Institute of Industrial Technology (KEIT) grant funded by the Korean government (MOTIE) (00420534); by the Ministry of Culture, Sports and Tourism (MCST) of Korea and the Korea Creative Content Agency (KOCCA) as part of the Culture Technology (CT) Research & Development Program (RS-2024-00439361); by the Future Resource Research Program (2E33542) of KIST; and by the 2024 research Fund (1.240007.01 and 1.240010.01) of UNIST.

Author contributions: J.I.K., D.-H.K., and C.C. conceived the concept and designed the experiments. M.K.C., D.-H.K., and C.C. supervised the whole project. J.S.K., J.K., and H.C. prepared the heterostructures and fabricated the devices. J.I.K. performed optoelectronic measurements and device characterization. J.I.K. performed in-sensor processing and imaging demonstration with the devices. J.I.K., T.-M.C., Juy.P., and C.C. analyzed the experimental data and carried out simulations. J.I.K., C.C., D.-H.K., and M.K.C. wrote the paper. All the authors discussed the results and commented on the manuscript. **Competing interests:** The authors declare that they have no competing interests. **Data and materials availability:** All data needed to evaluate the conclusions in the paper are present in the paper and/or the Supplementary Materials. Data and code used for high-clarity contour extraction are also publicly available at https://doi.org/10.5061/dryad.bcc2fqzpt.

Submitted 6 October 2024
Accepted 28 March 2025
Published 2 May 2025
10.1126/sciadv.adt6527